This is the accepted manuscript made available via CHORUS. The article has been published as:

Exploring the role of high-math xmlns="http://www.w3.org/1998/Math/MathML">mi>j/mi>/math> configurations in collective observables through the Coulomb excitation of math xmlns="http://www.w3.org/1998/Math/MathML">mmultiscripts>mi>Cd/mi>mprescripts>/mprescripts>none>/none>mn>106/mn>/mmultiscripts>/math>

D. Rhodes, B. A. Brown, J. Henderson, A. Gade, J. Ash, P. C. Bender, R. Elder, B. Elman, M. Grinder, M. Hjorth-Jensen, H. Iwasaki, B. Longfellow, T. Mijatović, M. Spieker, D. Weisshaar, and C. Y. Wu

Phys. Rev. C **103**, L051301 — Published 13 May 2021

DOI: 10.1103/PhysRevC.103.L051301

Exploring the role of high-j configurations in collective observables through the Coulomb excitation of ^{106}Cd

D. Rhodes,[1,2,*] B. A. Brown,[1,2] J. Henderson,[3,4] A. Gade,[1,2] J. Ash,[1,2] P. C. Bender,[1,†] R. Elder,[1,2] B. Elman,[1,2] M. Grinder,[1,2] M. Hjorth-Jensen,[1,2,5] H. Iwasaki,[1,2] B. Longfellow,[1,2,‡] T. Mijatović,[1,§] M. Spieker,[1,¶] D. Weisshaar,[1] and C. Y. Wu[4]

[1]*National Superconducting Cyclotron Laboratory, Michigan State University, East Lansing, Michigan 48824, USA*
[2]*Department of Physics and Astronomy, Michigan State University, East Lansing, Michigan 48824, USA*
[3]*Department of Physics, University of Surrey, Guildford, Surrey GU2 7XH, United Kingdom*
[4]*Lawrence Livermore National Laboratory, Livermore, CA 94550, USA*
[5]*Department of Physics and Center for Computing in Science Education, University of Oslo, Oslo, Norway.*

(Dated: April 21, 2021)

The shape and collectivity of ^{106}Cd was investigated via a sub-barrier-energy Coulomb excitation experiment performed at the NSCL ReA3 facility using the JANUS setup. Transition matrix elements between low-lying states were found to agree with adopted values, and information on the shape and collectivity of higher-lying states was extracted for the first time. Locally-optimized large-scale shell-model calculations were found to describe well the $B(E2)$ transition strengths but failed to reproduce the spectroscopic quadrupole moments Q_s. An analysis of the $E2$ rotational invariants and the normalized quadrupole moment q_s indicates that this may be due to a significant degree of triaxiality in ^{106}Cd which is not captured by the present shell-model calculations. Analogous calculations for the Fe isotopes (two protons below the $Z = 28$ magic number) reveal the critical role of high-j neutron configurations for the description of quadrupole moments in the heavy Fe and Cd isotopes (two protons below magic $Z = 50$), but this effect is insufficient to explain the shape of ^{106}Cd, posing a puzzle for the understanding of nuclear structure towards $N = 50$.

In even-even nuclei, the electromagnetic $B(E2; 2_1^+ \rightarrow 0_1^+)$ transition strength is a measure of quadrupole collectivity, sensitive to shell-breaking effects, nuclear deformation, and nucleon-nucleon correlations. Studies of collective properties in nuclei near $N = Z = 50$ ^{100}Sn, the heaviest self-conjugate doubly-magic nucleus known to exist, have revealed one of the most persistent puzzles in rare-isotope science. In the Sn isotopes, this transition strength has been reported from ^{104}Sn [1] to ^{132}Sn [2], spanning a chain of 15 even-even Sn isotopes. The trend is asymmetric about mid-shell with enhanced collectivity towards ^{100}Sn (see Ref [1] and references therein).

Evidence has been mounting that the origin of this unusual behavior lies in proton excitations across the $Z = 50$ shell gap [1, 3, 4]. Perhaps surprisingly, there is no such evidence in the $Z = 48$ Cd isotopic chain. Rather, the $B(E2)$ transition strengths smoothly decrease from mid-shell to ^{102}Cd, in agreement with conventional large-scale shell-model calculations [5]. However, in the present work, we explore the importance of high-j orbitals for the description of quadrupole moments and triaxiality in Cd isotopes with $N \geq 60$ and demonstrate that this effect is not sufficient to explain the shape of the $N < 60$ Cd isotopes which are just two protons below Sn. Such higher-order indicators of shape and collectivity are accessible with high-statistics sub-barrier Coulomb excitation which is reported here for the rare but stable ^{106}Cd isotope.

The known information on the lowest-lying levels in ^{106}Cd primarily stems from two Coulomb excitation experiments performed in the 1960s and 70s [6, 7]. More recently, an excited state g-factor measurement on ^{106}Cd [8] allowed for the extraction of lifetimes via the Doppler-Shift-Attenuation method from the observed, prominent γ-ray lineshapes. These excited-state lifetimes, however, disagree with the adopted values from Coulomb excitation. Most significantly, the lifetime reported for the 2_1^+ state is 33% below the previous literature value, which would imply a significant increase in the ^{106}Cd $B(E2)$ transition strength. This increased collectivity is at odds with large-scale shell-model calculations which were in good agreement with the adopted values [5].

To extend the existing information on collectivity and shape to states previously out of reach, and to address the discrepancies that appeared with the most recent measurement, an inverse-kinematics sub-barrier-energy Coulomb excitation experiment was performed on ^{106}Cd using the highest-Z probe yet and, for the first time, modern particle and γ-ray detection arrays.

The experiment was performed at the Re-accelerator facility (ReA3) [9] of the National Superconducting Cyclotron Laboratory (NSCL) [10]. The stable ^{106}Cd nuclei were vaporized and injected into the NSCL's electron-beam ion trap [11] where they were charge bred to 37+ and injected into the ReA3 linear accelerator. The ions were accelerated to the desired energies and delivered to the experimental setup located at the ReA3 general pur-

* rhodesd@nscl.msu.edu
† Present address: Department of Physics, University of Massachusetts Lowell, Lowell, Massachusetts 01854, USA.
‡ Present address: Lawrence Livermore National Laboratory, 7000 East Ave., Livermore, CA 94550, USA.
§ Present address: Division of Experimental Physics, Ruder Bokovi Institute, Bijenika cesta 54, 10000 Zagreb, Croatia
¶ Present address: Department of Physics, Florida State University, Tallahassee, Florida 32306, USA.

pose beamline.

The experiment consisted of three separate settings. In two settings, the ^{106}Cd beam was impinged on a 0.92-mg/cm^2 ^{208}Pb target at 4.36 and 4.03 MeV/u. The third setting scattered the ^{106}Cd beam at 3.0 MeV/u off a 0.98-mg/cm^2 ^{48}Ti target. The two different beam energies used on ^{208}Pb enhance the sensitivity to the nuclear matrix elements, while the ^{48}Ti target primarily provided an absolute normalization through the observed target excitations.

The target position was surrounded by the Joint Array for Nuclear Structure (JANUS) [12], which combines two annular silicon detectors with the Segmented Germanium Array (SeGA) [13]. The JANUS silicon detectors were placed 26(1) mm downstream and 34(1) mm upstream of the reaction target. They have 32-fold azimuthal segmentation on the side facing the target and 24-fold radial segmentation on the other. This geometry covers LAB frame scattering angles of $22.9° - 53.4°$ (downstream) and $136° - 163°$ (upstream) with $\approx 1°$ localization in θ and $11.3°$ in ϕ. The silicon detectors were used to detect the scattered ^{106}Cd and the recoiling ^{208}Pb or ^{48}Ti target nuclei (either independently or in coincidence depending on the scattering angle).

Sixteen 32-fold segmented detectors of SeGA were arranged in a compact "barrel" configuration, with the cylindrical detector crystals concentrically surrounding the target position. These were used to detect the prompt γ-ray decays from excited states of both nuclei and provide an absolute efficiency of 6.7% at 1 MeV.

The energy deposited in the forward silicon detector during the higher-energy setting on ^{208}Pb is shown in Fig. 1. As is clearly seen, the kinematic curves of the scattered ^{106}Cd and the ^{208}Pb target recoils are well separated; this allows for unambiguous event-by-event particle identification and characterization of the scattering process.

To increase the sensitivity of the measurement, the data were further subdivided into ranges of scattering angles. For the high-energy setting on ^{208}Pb, the forward-scattered ^{106}Cd projectiles were divided into four angular ranges, the ^{208}Pb recoils were divided into two ranges, and back-scattered ^{106}Cd was considered as a whole. For the low-energy setting on ^{208}Pb, the forward-scattered ^{106}Cd projectiles were divided into three angle ranges; the division of the ^{208}Pb and back-scattered ^{106}Cd events was the same as in the high-energy setting. For the ^{48}Ti target, only the target recoils were selected to tag the Coulomb excitation process due to the particular kinematics of the reaction. This data was divided into five angular ranges.

The choice of angular ranges was primarily motivated by the γ-ray statistics observed in each setting. The total γ-ray spectra collected in coincidence with Si events for all settings are shown in Fig. 2. The Doppler correction is enabled by the high segmentation of SeGA and the JANUS Si detectors as well as by the known two-body reaction kinematics for each setting.

The ^{48}Ti target contained a 3.1% (by mass)

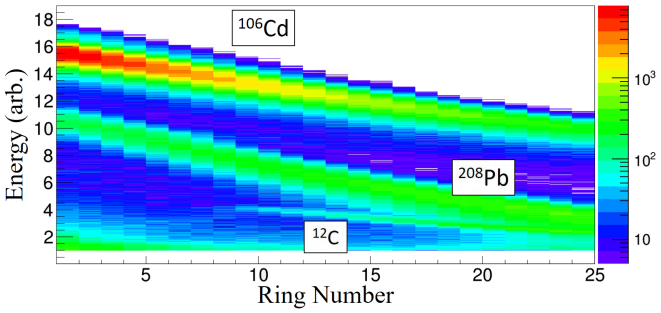


FIG. 1. Energy deposited in the forward silicon detector during the setting with ^{106}Cd at 4.36 MeV/u on ^{208}Pb. The scattered ^{106}Cd and recoiling ^{208}Pb nuclei are clearly visible and distinguishable, as are ^{12}C nuclei which come from a thin supportive backing on the target. Note that, for clarity, bins with 5 or fewer counts are excluded and a low-energy threshold has been applied.

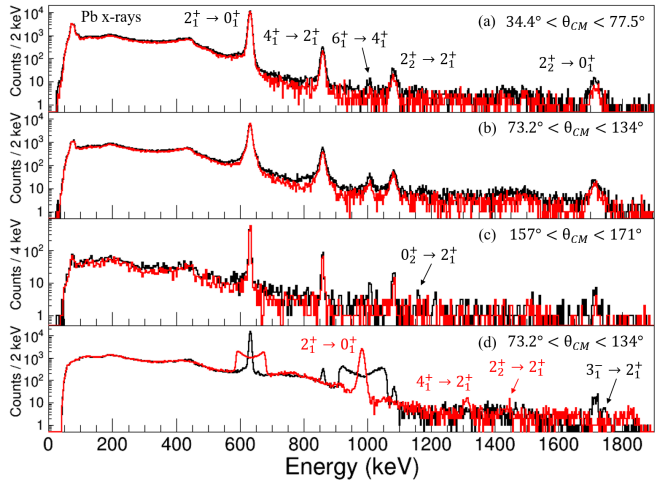


FIG. 2. Total Doppler-corrected γ-ray spectra collected during the experiment. Panels (a)-(c) show the ^{208}Pb target data, with the higher energy setting in black and lower energy setting in red. The three scattering regions correspond to forward-scattered ^{106}Cd (a), recoiling ^{208}Pb (b), and back-scattered ^{106}Cd (c). Panel (d) shows the data on ^{48}Ti. The black spectrum is Doppler corrected for ^{106}Cd, the red spectrum for ^{48}Ti. The observed γ-ray transitions are indicated in black for ^{106}Cd and red for ^{48}Ti.

^{182,184,186}W contamination. Due to the larger mass of tungsten, ^{106}Cd nuclei scattered by the contaminants were separable using the silicon detectors and thus this did not impact the analysis.

The γ-ray yield data were analyzed through a joint use of the GOSIA and GOSIA2 codes [14, 15]. The level schemes and literature data employed during the analysis for both nuclei are given in the Supplemental Material [16]. Initially, the data collected on the ^{48}Ti target was analyzed independently using the Coulomb excitation code GOSIA2, which was developed specifically for a simultaneous analysis of projectile and target excitations. The well-known spectroscopic data for the low-lying states in ^{48}Ti, combined with its measured γ-

ray yields, provide an absolute normalization for the observed ^{106}Cd excitations. The matrix elements of ^{106}Cd can be determined relative to this normalization.

During the GOSIA2 analysis, the ^{106}Cd $\langle 0_1^+ \| E2 \| 2_1^+ \rangle$ and $\langle 2_1^+ \| E2 \| 2_1^+ \rangle$ matrix elements were scanned, while all other matrix elements in ^{106}Cd were fixed. This results in a two-dimensional χ^2 surface, with the best-fit matrix elements given at the minimum χ^2 value and the 1σ uncertainties given by a $\chi^2 < \chi^2_{min} + 1$ cut. No literature constraints for ^{106}Cd were used in this step of the analysis.

The best-fit $\langle 0_1^+ \| E2 \| 2_1^+ \rangle$ matrix element and its uncertainty is then provided as an additional data point to a full GOSIA minimization which considers all three settings and the literature constraints for ^{106}Cd given in the Supplemental Material [16]. We note that the $\langle 0_1^+ \| E2 \| 2_1^+ \rangle$ matrix element is not fixed for this step. This is because, during the GOSIA2 analysis, the matrix elements which couple to states beyond the 2_1^+ were not correct as they had not yet been determined. These incorrect couplings have an effect on the best-fit $\langle 0_1^+ \| E2 \| 2_1^+ \rangle$ matrix element extracted from GOSIA2, and thus this matrix element should be allowed to vary during the full GOSIA minimization in order to find a solution which best balances the GOSIA2 constraint with all three data sets.

After convergence of the full GOSIA fit, the χ^2 surface is recreated; the matrix elements which couple to higher-lying states are now fixed at the values determined by the previous full GOSIA fit. The (more accurate) $\langle 0_1^+ \| E2 \| 2_1^+ \rangle$ matrix element from this new surface is then provided once again to a full GOSIA minimization, and this process is iterated until the results have converged [15].

The matrix elements extracted from this analysis are shown in Table I, and the corresponding exited state lifetimes are shown in Table II. The quoted uncertainties have been symmetrized and are the result of combining statistical and systematic effects. The dominant systematic error arises from the 1 mm ($\approx 3-4\%$) uncertainty on the separation between the reaction target and the silicon detectors.

As is apparent from Tables I and II, the present work agrees well with the original Coulomb excitation data [6, 7] for all states observed, strongly supporting the adopted values over the discrepant results reported in [8].

Large-scale shell-model calculations were performed to understand both the shape and collectivity of ^{106}Cd. A model space and Hamiltonian of a form similar to [5] was employed; this is based on an ^{88}Sr core with the valence $(1p_{1/2}, 0g_{9/2})$ orbitals for protons and the $(0g_{7/2}, 1d_{5/2}, 1d_{3/2}, 2s_{1/2}, 0h_{11/2})$ orbitals for neutrons. Effective charges of $e_p = 1.6$ and $e_n = 1.0$ were used.

The calculations were carried out with the NuShellX code [19], and they reproduce well the $B(E2; 2_1^+ \rightarrow 0_1^+)$ values of Table VI in [5] for ^{102,104}Cd. In order to run the ^{106}Cd calculation, a truncation of the neutron configurations was made allowing at most two neutrons in the $0h_{11/2}$ orbital. The resulting energies are within 50 keV of those in [5], and the $B(E2; 2_1^+ \rightarrow 0_1^+)$ also agrees. For all three nuclei, the quadrupole moments Q_s from our shell-model calculations are larger by a factor of roughly 2.2 over those in [5] due to an incorrect normalization applied in [5].

Calculated transition strengths and quadrupole moments are compared to the experimentally determined values in Table III. The Sr88 shell-model calculations reproduce the transition strengths in the ground-state band rather well, but it is clear the quadrupole moments are much less well described; the calculated $Q_s(2_1^+)$ is larger than the experimental value by roughly a factor of three.

Due to the number of well-determined matrix elements extracted from this work, a comparison of the quadrupole rotational invariants $\langle Q^2 \rangle$ and $\langle Q^3 \cos 3\delta \rangle$ [20, 21] can be made in order to further explore the discrepancies between experiment and theory presented in Table III. The model-independent parameters (Q, δ) determine the

TABLE I. Matrix elements extracted from the present analysis compared to literature values.

$\langle J_i^\pi \| E2 \| J_f^\pi \rangle$ [eb]						
J_i^π	J_f^π	This Work	Ref [8]	Ref [6]	Ref [7]	Ref [17]
0_1^+	2_1^+	0.652(11)	0.76(3)	0.653(13)	0.620(3)	-
2_1^+	2_1^+	-0.25(5)	-	-	-0.37(11)	-
2_1^+	4_1^+	1.044(25)	0.79(2)	1.11(7)	-	-
4_1^+	4_1^+	-0.52(24)	-	-	-	-
4_1^+	6_1^+	1.37(10)	-	-	-	-
6_1^+	6_1^+	-1.3(8)	-	-	-	-
0_1^+	2_2^+	0.169(4)	-	0.190(13)	-	-
2_1^+	2_2^+	0.415(15)	-	0.49(4)	-	0.32(5)
2_2^+	2_2^+	1.33(6)	-	-	-	-
$\langle J_i^\pi \| M1 \| J_f^\pi \rangle$ [μ_N]						
J_i^π	J_f^π	This Work	Ref [6]	Ref [17]		
2_1^+	2_2^+	-0.263(17)	-0.39	-0.35(5)		
$\langle J_i^\pi \| E3 \| J_f^\pi \rangle$ [$eb^{\frac{3}{2}}$]						
J_i^π	J_f^π	This Work	Ref [18]			
0_1^+	3_1^-	0.28(14)	0.40(5)			

TABLE II. Excited state lifetimes extracted from the present analysis compared to literature values. Since no literature lifetimes were used to constrain the GOSIA minimization, these results are independent of previous measurements.

Lifetime τ [ps]					
State	This Work	Ref [8]	Ref [6]	Ref [7]	Ref [27]
2_1^+	9.5(3)	7.0(3)	9.4(4)	10.49(12)	9.9(12)
4_1^+	1.42(7)	2.5(2)	1.26(16)	-	-
6_1^+	0.54(8)	-	-	-	-
2_2^+	0.50(3)	0.28(2)	0.45(7)	-	-

TABLE III. Transition strengths and spectroscopic quadrupole moments determined from this work compared to shell-model predictions.

$B(E2; J_i^\pi \to J_f^\pi)$ $[e^2b^2]$				
J_i^π	J_f^π	Experiment	jj45	Sr88
2_1^+	0_1^+	0.085(3)	0.0933	0.0774
4_1^+	2_1^+	0.121(6)	0.134	0.111
6_1^+	4_1^+	0.145(21)	0.104	0.0906
2_2^+	0_1^+	$5.7(3) \times 10^{-3}$	8.65×10^{-6}	4.72×10^{-4}
2_2^+	2_1^+	0.0345(25)	7.63×10^{-6}	7.27×10^{-4}
2_3^+	0_1^+	-	3.46×10^{-3}	2.76×10^{-3}
2_3^+	2_1^+	-	0.0103	7.82×10^{-3}

Spectroscopic Quadrupole Moment Q_s [eb]			
State	Experiment	jj45	Sr88
2_1^+	-0.19(4)	-0.603	-0.550
4_1^+	-0.39(18)	-0.760	-0.687
6_1^+	-0.8(5)	-0.563	-0.549
2_2^+	1.01(5)	-0.345	-0.205
2_3^+	-	0.611	0.4055

magnitude and character, respectively, of the quadrupole deformation of the charge distribution in the intrinsic frame.

Only the two lowest-order rotational invariants are considered here. See, for example, Refs [21, 22] for a discussion of higher-order invariants. Special attention is paid to the "normalized" quadrupole moment q_s, which is closely related to an approximation of the quadrupole asymmetry invariant $\langle \cos 3\delta \rangle$ via

$$q_s = -\langle \cos 3\delta \rangle_{2_1^+} = \frac{Q_s(2_1^+)}{\frac{2}{7}\sqrt{\frac{16\pi}{5}B(E2; 0_1^+ \to 2_1^+)}}. \qquad (1)$$

Specifically, $\langle \cos 3\delta \rangle_{2_1^+}$ is the quadrupole asymmetry when only the 2_1^+ excited state is considered.

The ratio q_s describes the size of the spectroscopic quadrupole moment $Q_s(2_1^+)$ relative to the prediction of the Bohr collective model. The values $q_s = -1, 1$ indicate prolate and oblate deformations, respectively, while all intermediate values $-1 < q_s < 1$ imply triaxiality. A comparison of the experimental and theoretical rotational invariants, as well as the particularly important contribution q_s, is shown in Table IV.

The very good reproduction of the $\langle Q^2 \rangle$ invariant by the shell model implies that the magnitude of the deformation is well described. However, the disagreement in both $\langle \cos 3\delta \rangle$ and q_s indicates that the type of deformation (or shape) is less well characterized; both measures imply a significant degree of triaxiality for ^{106}Cd which appears not to emerge from the shell-model calculations.

Calculated values of q_s for Cd isotopes and $N = 58$ isotones compared to experimental values are presented in Fig. 3. The data for ^{102,104}Cd were taken from Table V of Ref [5], while all other literature data are taken from NNDC/ENSDF.

TABLE IV. The ^{106}Cd ground state rotational invariants and normalized quadrupole moments determined from this work compared to shell-model calculations. The quoted uncertainties are purely experimental (see Table I). The quadrupole asymmetry $\langle \cos 3\delta \rangle$ was estimated as in [23–25].

Ground State Rotational Invariants			
Invariant	Experiment	jj45	Sr88
$\langle Q^2 \rangle$ $[e^2b^2]$	0.454(14)	0.484	0.403
$\langle Q^3 \cos 3\delta \rangle$ $[e^3b^3]$	-0.02(2)	0.265	0.198
$\langle \cos 3\delta \rangle$	-0.06(6)	0.79	0.78

Normalized Quadrupole Moment q_s			
Experiment	jj45	Sr88	Ref [26]
-0.32(6)	-0.975	-0.976	-0.72

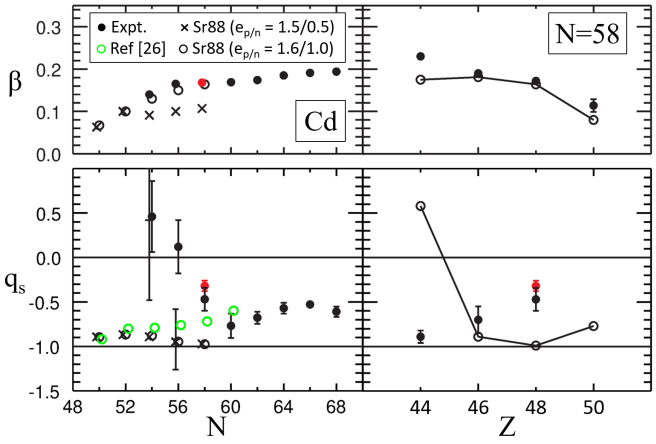


FIG. 3. Calculated values of q_s (bottom) and quadrupole deformation β (top) compared to experimental values for Cd isotopes (left) and $N = 58$ isotones (right). The experimental values from this work are in red. The green circles are shell-model calculations from Ref [26].

The discrepancy with experiment for the ^{106}Cd q_s cannot be accounted for within the Sr88 model space. Repeating the calculations in the expanded jj45 model space, which includes the $(0f_{5/2}, 1p_{3/2}, 1p_{1/2}, 0g_{9/2})$ proton orbitals, q_s is still close to -1 (see Table IV). Unlike the overall deformation, q_s is insensitive to the effective charges since these factors mostly cancel in the ratio of Eq. 1 (see Fig. 3); thus the discrepancy in q_s cannot be improved by adjusting the effective charges.

The total effective charge is $e_p = 1 + \delta e_p(high) + \delta e_p(low)$ and $e_n = \delta e_n(high) + \delta e_n(low)$. The $\delta e(high)$ take into account the core-polarization from $2\hbar\omega$ $1p-1h$ admixtures that are connected to the giant quadrupole resonance. Typical empirical values in the *sd* [28] and *fp* [29] model spaces are close to $\delta e_p(high) = \delta e_n(high) = 0.5$. The additional $\delta e(low)$ are introduced to compensate for the truncation within the $0hw$

shell, in particular, the lack of proton excitations from $0g_{9/2}$ to $(0g_{7/2}, 1d_{5/2}, 1d_{3/2}, 2s_{1/2})$. In our case, we used $\delta e_p(low) = 0.1$ and $\delta e_n(low) = 0.5$.

It is interesting to compare the results for Cd ($Z = 48$) to those for Fe ($Z = 26$); these are shown in Fig. 4. Results for Fe are obtained with the $f7j4$ model space which consists of $0f_{7/2}$ for protons and $(0f_{5/2}, 1p_{3/2}, 1p_{1/2}, 0g_{9/2})$ for neutrons. This is analogous to the Sr88 model space for Cd. As can be seen again, effective charges larger than e(high) are required to reproduce the experimental deformation.

Both the fp model space with $e(high)$ and the $f7j4$ model space with $e(high)$+$e(low)$ give $q_s \approx -1$ from $N = 28-34$. And for $N = 30, 32$ this agrees with experiment. Thus, the increase in q_s observed for ^{106}Cd compared to the results of the Sr88 model space is not likely due to the major-shell truncation.

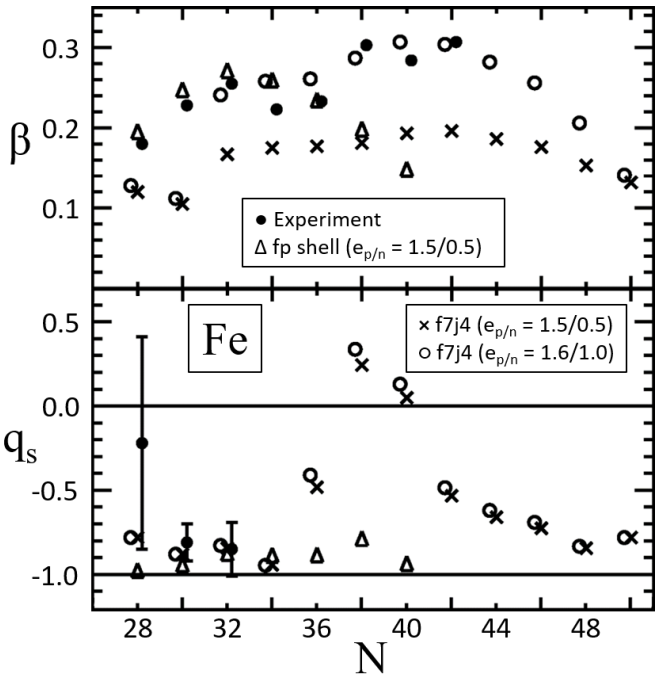


FIG. 4. Calculated values of q_s (bottom) and quadrupole deformation β (top) compared to experimental values for Fe. The experimental data is from Ref [30].

The $f7j4$ results for Fe reveal the reason for a change in q_s at large N. We find the q_s values for high-j configurations j^n are very simple. They are $q_s \approx +1$ for $n = 2$ and $q_s \approx -1$ for $n = -2$, with a nearly linear decrease in between. For both Fe and Cd, the protons are in a state with $n = -2$. Thus, the result for q_s as a function of N is determined by a constant $q_s \approx -1$ contribution from the protons combined with a varying q_s contribution from the neutrons which depends on the occupancy of the $0g_{9/2}$ neutron orbital in Fe. In fact, the role of high-j configurations in determining nuclear shape in well-deformed nuclei is a much-explored phenomenon [31–33].

The impact of the neutron $0h_{11/2}$ orbital on the shape of Cd isotopes can be seen in Fig. 3. The data for $N \geq 60$ show a smooth increase in q_s out to mid-shell, in line with the expectations set by the Fe calculations, though the effect is less pronounced in Cd. The calculations from Ref [26], which are also based on an ^{88}Sr core but make no truncation of the neutron $0h_{11/2}$, show an increase in q_s for all isotopes and give good agreement at $N = 60$. The calculated q_s values from Ref [26] are larger than those from this work due to the location of the $0h_{11/2}$ single-particle energy. For ^{101}Sn the $0h_{11/2}$ orbital comes at an excitation energy of 6.76 MeV with our Sr88 interaction; it comes at 2.47 MeV with the interaction from [26]. Thus the admixture of $0h_{11/2}$ is larger in the wave-functions from [26] compared to ours.

What is striking is the rapid increase in the experimental q_s with decreasing N starting at $N = 58$ compared to the calculations. This cannot be explained by the calculations presented in this paper. To explore this discrepancy further, similar calculations were performed for $N = 58$ isotones (Fig. 3, right). The data show a clear increase of q_s with increasing Z. Again, the calculations presented in this work do not offer an explanation; the calculated q_s show the impact of the high-j proton configurations discussed earlier. The $Z = 44$ q_s calculation may be too high due to the current model space not being appropriate for ruthenium; however, it is not likely that the experimental value would be reproduced even with an optimized model space.

These observations suggests several further investigations. Measurements of q_s in heavy Cd and Fe nuclei could confirm the similarity of the two isotopic chains, and shell-model calculations which fully incorporate the neutron $0h_{11/2}$ for all heavy Cd isotopes could quantify the effect of this critical high-j orbital in Cd. Further, precise measurements of q_s in $^{100-104}$Cd, as well the $N = 58$ nucleus ^{108}Sn, could determine whether the trends observed in Fig. 3 continue. If so, it would represent a major deviation from the configuration-interaction based models presented here in a critical region of the nuclear chart near ^{100}Sn.

In summary, a sub-barrier-energy Coulomb excitation experiment on ^{106}Cd was performed at the NSCL ReA3 facility using the JANUS setup. The extracted transition matrix elements and excited-state lifetimes agree well with the adopted values [6, 7] which are at odds with a more recent measurement [8]. Large-scale shell-model calculations performed for comparison describe well the $B(E2)$ transition strengths, but they fail to reproduce the quadrupole moments. An analysis of $E2$ rotational invariants extracted from experiment, including the particularly important quantity q_s, reveals a significant degree of triaxiality in ^{106}Cd which appears not to emerge from the present shell-model calculations. We show that this discrepancy cannot be reconciled within the Hamiltonians presently at hand, and that it cannot be fixed by changing the effective charges. A comparison with analogous calculations for the Fe isotopes, two protons below Ni, show that high-j neutron configurations cause the increase of q_s for Cd isotopes with $N \geq 60$, but they also show that this effect cannot explain the current result for ^{106}Cd. The existing data for the light Cd isotopes and

the $N = 58$ isotones with $Z \geq 44$ hint at a striking deviation from the presented shell-model calculations; this motivates similar measurements for more neutron-deficient Cd and Sn isotopes to explore the unexpected evolution of quadrupole moments in this critical region of the nuclear chart.

ACKNOWLEDGMENTS

Helpful discussions with L. P. Gaffney are gratefully acknowledged. We also thank G. W. Severin and H. K. Clause for an ICP-OES analysis of the ^{48}Ti target. This work was supported by the U.S. Department of Energy, Office of Science, Office of Nuclear Physics, under Grant No. DE-SC0020451, the U.S. National Science Foundation (NSF) under Grant No. PHY-1565546, and by the DOE National Nuclear Security Administration through the Nuclear Science and Security Consortium, under Award No. DE-NA0003180. B.A.B. acknowledges support from NSF Grant No. PHY-1811855. M. H. acknowledges support from NSF Grant No. 2013047 and from DOE Grant No. DE-SC0021152. Work at LLNL was performed under contract DE-AC52-07NA27344. Work at the University of Surrey was supported under UKRI Future Leaders Fellowship grant no. MR/T022264/1

[1] V. M. Bader *et al.*, Phys. Rev. C 88, 051301(R) (2013).
[2] D. Rosiak *et al.*, Phys. Rev. Lett. 121, 252501 (2018).
[3] A. Banu *et al.*, Phys. Rev. C **72**, 061305(R), (2005).
[4] T. Togashi *et al.*, Phys. Rev. Lett. 121, 062501 (2018).
[5] A. Ekström *et al.*, Phys. Rev. C **80**, 054302 (2009).
[6] W. T. Milner *et al.*, Nucl. Phys. A **129**, 687 (1969).
[7] M. T. Esat *et al.*, Nucl. Phys. A **274**, 237 (1976).
[8] N. Benczer-Koller *et al.*, Phys. Rev. C **94**, 034303 (2016).
[9] A. C. C. Villari *et al.*, in *Proceedings of International Particle Accelerator Conference (IPAC'16), Busan, Korea, 2016*, pp. 1287-1290.
[10] A. Gade and B. M. Sherrill, Phys. Scr. **91**, 053003 (2016).
[11] A. Lapierre *et al.*, Phys. Rev. Accel. Beams **21**, 053401 (2018).
[12] E. Lunderberg *et al.*, Nucl. Instrum. and Meth. in Phys. Res. A **885**, 30 (2018).
[13] W.F. Mueller *et al.*, Nucl. Instrum. and Meth. in Phys. Res. A **466**, 492 (2001).
[14] T. Czosnyka *et al.*, Bull. Am. Phys. Soc. **28**, 745 (1983).
[15] M. Zielinska *et al.*, Eur. Phys. J. A **52**, 99 (2016).
[16] See Supplemental Material at for literature data and level schemes employed during the analysis.
[17] Z. W. Grabowski and R. L. Robinson, Nucl. Phys. A **206**, 633 (1973).
[18] M. P. Fewell *et al.*, Aust. J. Phys. **38**, 555 (1985).
[19] B. A. Brown and W. D. M. Rae, Nuclear Data Sheets **120**, 115 (2014).
[20] K. Kumar, Phys. Rev. Lett. **28**, 249 (1972).
[21] D. Cline, Ann. Rev. Nucl. Part. Sci. **36**, 683 (1986).
[22] J. Henderson, Phys. Rev. C **102**, 054306 (2020).
[23] J. Srebrny *et al.*, Nucl. Phys. A **766**, 25 (2006).
[24] K. Wrzosek-Lipska *et al.*, Phys. Rev. C **86**, 064305 (2012).
[25] J. Henderson *et al.*, Phys. Rev. C **99**, 054313 (2019).
[26] T. Schmidt *et al.*, Phys. Rev. C **96**, 014302 (2017).
[27] J. Zhong *et al.*, Chinese Phys. C **44**, 094001 (2020).
[28] W. A. Richter *et al.*, Phys. Rev. C **78**, 064302 (2008).
[29] M. Honma *et al.*, Phys. Rev. C **69**, 034335 (2004).
[30] Y. Y. Sharon *et al.*, Nucl. Phys. A **980**, 131 (2018).
[31] S. Frauendorf and F. R. May, Phys. Lett. B **125**, 245 (1983).
[32] I. Hamamoto and B. R. Mottelson, Phys. Lett. B **127**, 281 (1983).
[33] I. Hamamoto, Phys. Lett. B **143**, 31 (1984).